Revista Minelor – Mining Revue
ISSN-L 1220-2053 / ISSN 2247-8590
vol. 29, issue 1 / 2023, pp. 26-41

CONTINUOUS MONITORING OF THE MINING ACTIVITIES, RESTORATION VEGETATION STATUS AND SOLAR FARM GROWTH IN COAL MINE REGION USING REMOTE SENSING DATA

Vancho ADJISKI[1], Václav ZUBÍČEK[2]*

[1]Faculty of Natural and Technical Sciences, "Goce Delchev" University, Shtip, R. N. Macedonia
[2]Department of Mining Engineering and Safety, Faculty of Mining and Geology,
VŠB-Technical University of Ostrava, Czech Republic

DOI: 10.2478/minrv-2023-0003

Abstract: *Land reclamation of previously mined regions has been incorporated in the mining process as awareness of environmental protection has grown. In this study, we used the open-pit coal mine Oslomej in R. N. Macedonia to demonstrate the activities related to the monitoring process of the study area.*
We combined the Google Earth Engine (GEE) computing platform with the Landsat time-series data, Normalized Difference Vegetation Index (NDVI), Random Forest (RF) algorithm, and the LandTrendr algorithm to monitor the mining impacts, land reclamation, and the solar farm growth of the coalfield region between 1984 and 2021.
The data from the sequential Landsat archive that was used to construct the spatiotemporal variability of the NDVI over the Oslomej mine site (1984-2021) and the pixel-based trajectories from the LandTrendr algorithm were used to achieve accurate measurements and analysis of vegetation disturbances.
The different land use/land cover (LULC) classes herbaceous, water, mine, bare land, and solar farm in the Oslomej coalfield area were identified, and the effects of LULC changes on the mining environment were discussed. The RF classification algorithm was capable of separating these LULC classes with accuracies exceeding 90 %. We also validated our results using random sample points, field knowledge, imagery, and Google Earth.
Our methodology, which is based on GEE, effectively captured information on mining, reclamation, and solar farm change, providing annual data (maps and change attributes) that can help local planners, policymakers, and environmentalists to better understand environmental influences connected to the ongoing conversion of the mining areas.
Keywords: *coal mine, NDVI, LandTrendr algorithm, Google Earth engine, restoration of vegetation, solar farm*

1. Introduction

Mineral resources are in higher demand as a result of rapid economic and social growth [1]. Due to various human activities, the Earth's surface has changed dramatically. Sustainable mining has become a global priority, owing to the growing acceptance of mine closure as a means of returning land to a usable state after mining, such as for agriculture and tourism [2]. Abandoned mines are often the result of evasive mining closure methods, posing a serious hazard to human health, environmental stability, and agricultural operations. Pollution, ecological deterioration, and biodiversity loss have all been observed in mining sites around the world, thwarting sustainable development goals [3, 4, 5]. These activities have a variety of damaging environmental consequences, and many governments demand that mining-affected regions be restored [6, 7].

More recently, the R. N. Macedonia government passed the Law on Mineral Raw Materials (No.136/12 from 2012), requiring mining companies to rehabilitate their sites once operations had ceased.

* Corresponding author: Vancho Adjiski, Assoc.prof. PhD.eng., Faculty of Natural and Technical Sciences, "Goce Delchev" University, (st. Goce Delchev no. 69, Shtip, R. N. Macedonia, vanco.adziski@ugd.edu.mk)

In some areas of R. N. Macedonia, land-cover changes around large surface mines have already harmed the environment. Both sustainable and green mining necessitate ongoing monitoring of these changes in order to determine the long-term effects on the environment [8, 9, 10]. Remote sensing has emerged as the most effective and impartial approach for tackling this problem. It provides comprehensive coverage of the mining area and enables repeated observation using the United States Geological Survey (USGS) publicly available Landsat archive [11, 12, 13]. The spatial and spectral features in Landsat imagery can be used to map diverse types of vegetation using a variety of vegetation indices.

Recent research on tracking land change has moved their attention to a multi-temporal analysis utilizing the entire Landsat archive, which has images with continuous acquisitions spanning more than 40 years [14, 15, 16, 17, 18]. Examples include forestry applications and dynamic monitoring of quarries utilizing a combination of remotely sensed datasets and various vegetation indices.

For example, Hansen et al. [19] used Landsat data to map global forest loss and gain from 2000 to 2012 at a spatial resolution of 30 m, and the results show a consistent and pertinent record of forest change. Kennedy et al. [20] used a deep temporal stack of Landsat images from 1984 to 2004 and a conceptual framework for change detection to track the dynamics of forest disturbance with distinctive temporal signatures in spectral space.

Vegetation indices have been employed in numerous studies to quantify the surface disturbance caused by coal mining. For instance, a time series NDVI has been utilized to monitor the process of mining-related land degradation and recovery [21, 22]. Xiao et al. [23] mapped mining disturbances to grassland and land recovery in open-pit mining region between 2003 and 2019 using the GEE platform, time-series Landsat data, and the LandTrendr method. Furthermore, He et al. [24] created a dynamic map for the water restoration and subsidence ponding years in mining landscapes in China's eastern plain using Landsat imagery and GEE. In addition, some studies [25, 26] explored the different varieties of mine vegetation, as well as the relationship between mine vegetation growth and the surrounding soil and heavy metals, as well as the mine's ecological restoration. Recently, GEE [27] with its tremendous cloud computing ability, facilitated the temporal uses of the Landsat data archive, such as monitoring of mining boundaries, vegetation removal and land reclamation.

The main restoration initiative after mining operations ceased is to replant flora such as grasses, bushes, and trees in the mined sites, although other management options include converting the mined regions into solar power stations.

In this research, we analyzed the areal expansion of the Oslomej mine in R. N. Macedonia for over 36 years and demonstrated the restoration of the region into vegetation and solar farm, using remote sensing techniques. Our study demonstrates the value of freely available data and algorithms in conjunction with a GEE cloud-based computing platform. The methodology described in this study enables efficient extraction of the spatio-temporal processes of mining activities and reclamation, thus providing valuable data for sustainable mining production and land reclamation. Overall, we anticipate that users will be inspired to replicate our methodology, particularly in developing countries where it is of key importance to monitor the post-mining processes.

2. Materials and methodology

2.1. Study area

This study was carried out at the Oslomej coal mine, located in the western part of the R. N. Macedonia, near the village Oslomej, municipality of Kichevo (Figure 1). It is located in the Kichevo Valley, 5 km from the city of Kichevo. The mine site, which is 6.3 km^2, underwent significant change from 1980 to 2021 when it was in operation. From a geomorphological point of view, the area of the Oslomej deposit has an altitude of 650 - 700 m with a slightly wavy shape. To the west of the exploitation field are several hilly mountain peaks with an altitude of 700 to 900 m.

The Oslomej basin is filled with Pliocene sediments lying on the Paleozoic rocks and is represented by gravel, sands, clays, and a productive series represented by gray clays, sands, and coal seams. In the deeper layers of the Pliocene sediments, coal seams with a thickness of 5-12 m have been found. The average thickness of the waste rock over the coal seams for open-pit exploitation is around 40 m.

The study area is located in the warm continental zone in which a modified moderate continental climate prevails, which is conditioned by the presence of mountain massifs with an altitude above 1000 m.

The average annual air temperature is 10.7 °C with an average annual maximum air amplitude of 20.8 °C. The average annual relative humidity is 73 %.

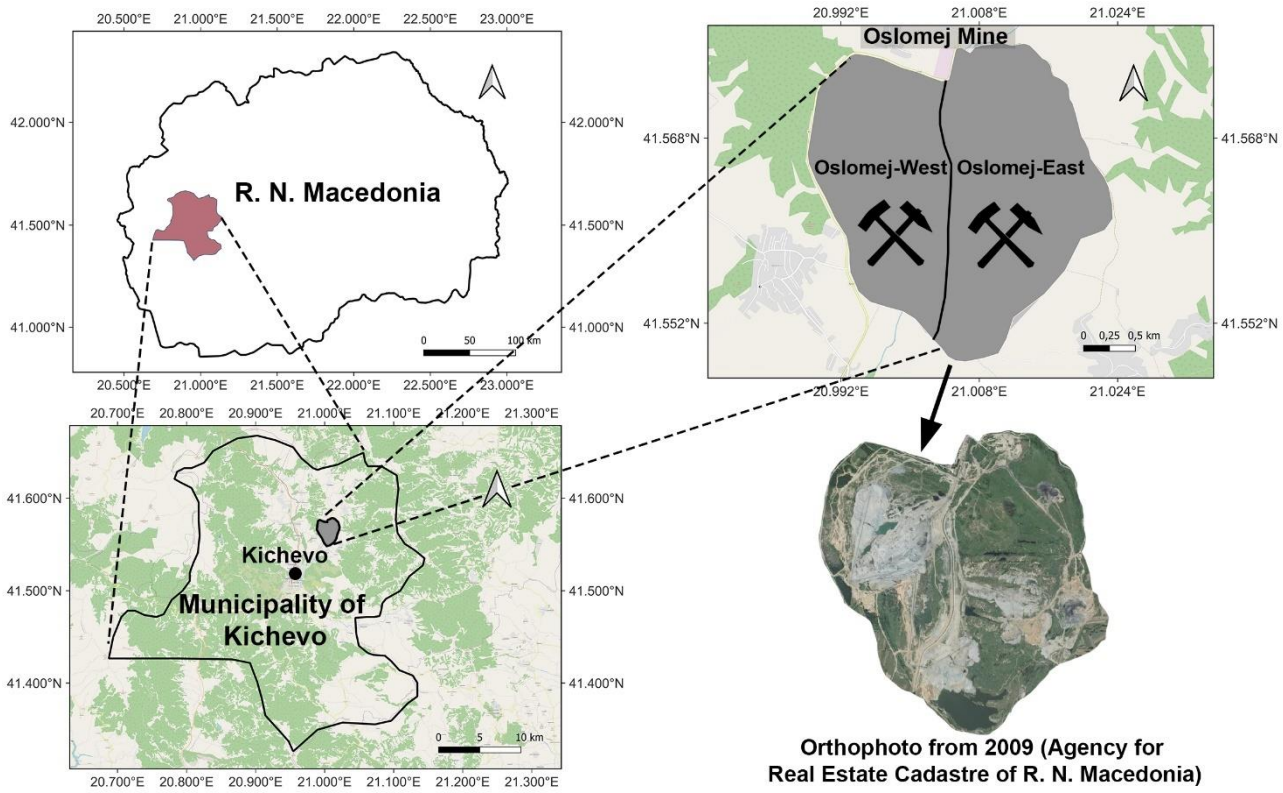

Figure 1. Location map of the study area

2.2. Overview of the methodology

Our approach is premised on the fact that abrupt changes in vegetation will occur as a result of open-pit mining and reclamation activities, as illustrated by the trajectory of the vegetation indices in Figure 2 [28, 29]. Monitoring of the open-pit mining progress was studied using time series analysis to detect breakpoints in the trajectories, indicating abrupt changes. Figure 3 displays the methodological framework used for this study.

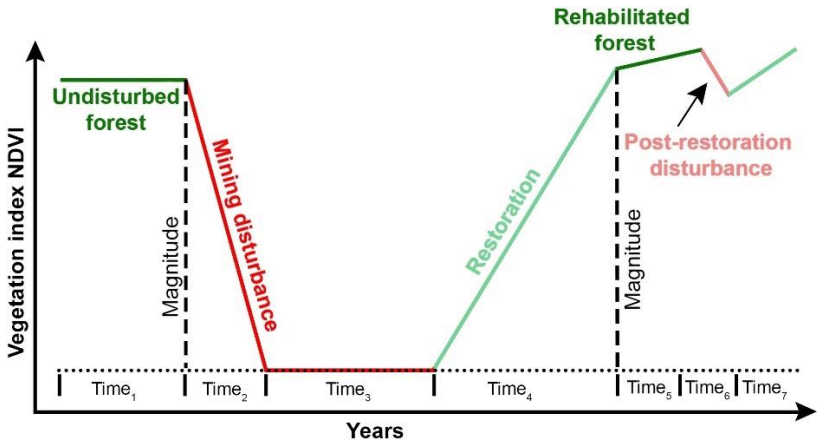

Figure 2. NDVI trajectory for predating, during, and postdating mining disturbances and restoration status

Using the JavaScript code editor from the GEE cloud computing platform, we accessed freely available Landsat scene collections from 1984 to 2021. The JavaScript code editor, which permits parallel computing and intensive data processing, was used to filter, and cloud mask those Landsat 5, 7, and 8 images at a resolution of 30 m.

Furthermore, the images had already been orthorectified and corrected for Level 1 Precision Terrain (L1TP) which satisfies both radiometric and geometric standards and is considered to be of the highest quality.

The conducted literature review shows that the NDVI is the most accurate indicator for identifying mine-induced vegetation changes [30, 31, 32, 33, 34]. For this purpose, we computed annual mean composites of this index for the collection of images from 1984 to 2021, to gain an overall understanding of the mine disturbance and recovery patterns. It is important to note that NDVI values were calculated as an average for

the entire Oslomej mine site. This is due to the fact that many mining companies do not always carry out rehabilitation initiatives simultaneously throughout the whole mining area. As a result, the overall recovery is taken into account by averaging the annual NDVI for the entire mining region. The equation for calculating NDVI is as follows: [35]:

$$\mathrm{NDVI} = \frac{\rho\mathrm{NIR} - \rho\mathrm{NIR}}{\rho\mathrm{Red} + \rho\mathrm{NIR}} \quad (1)$$

where ρNIR and ρNIR are the surface reflection values in the near-infrared and red range of the electromagnetic spectrum, respectively. The NDVI ranges from -1 to 1, with negative values reflecting a lack of vegetation and positive values denoting areas with vegetation.

We applied the RF classifier to Landsat images in GEE to classify the mine areas in order to fulfill the stated goals of this study. The classified maps of the years 1984, 1989, 1994, 1999, 2004, 2009, 2014, 2019, 2020 and 2021 were produced with the appropriate LULC classes. The study also provides the spatial distribution, area statistics, and the magnitude of change in different LULC categories during the selected years.

In this study, we also used the GEE platform to run the LandTrendr algorithm that can extract time-series images data obtained by Landsat sensors. This algorithm can process each pixel's time series to simplify their spatiotemporal trajectory from 1984 to 2021. To show how different areas of the mine are reclaimed, we used the LandTrendr algorithm to evaluate patterns of disturbance and recovery in selected portions of the mine site.

Finally, the method's accuracy was determined. The GEE platform was used for the majority of operations. Maps were generated and visualized in Qgis.

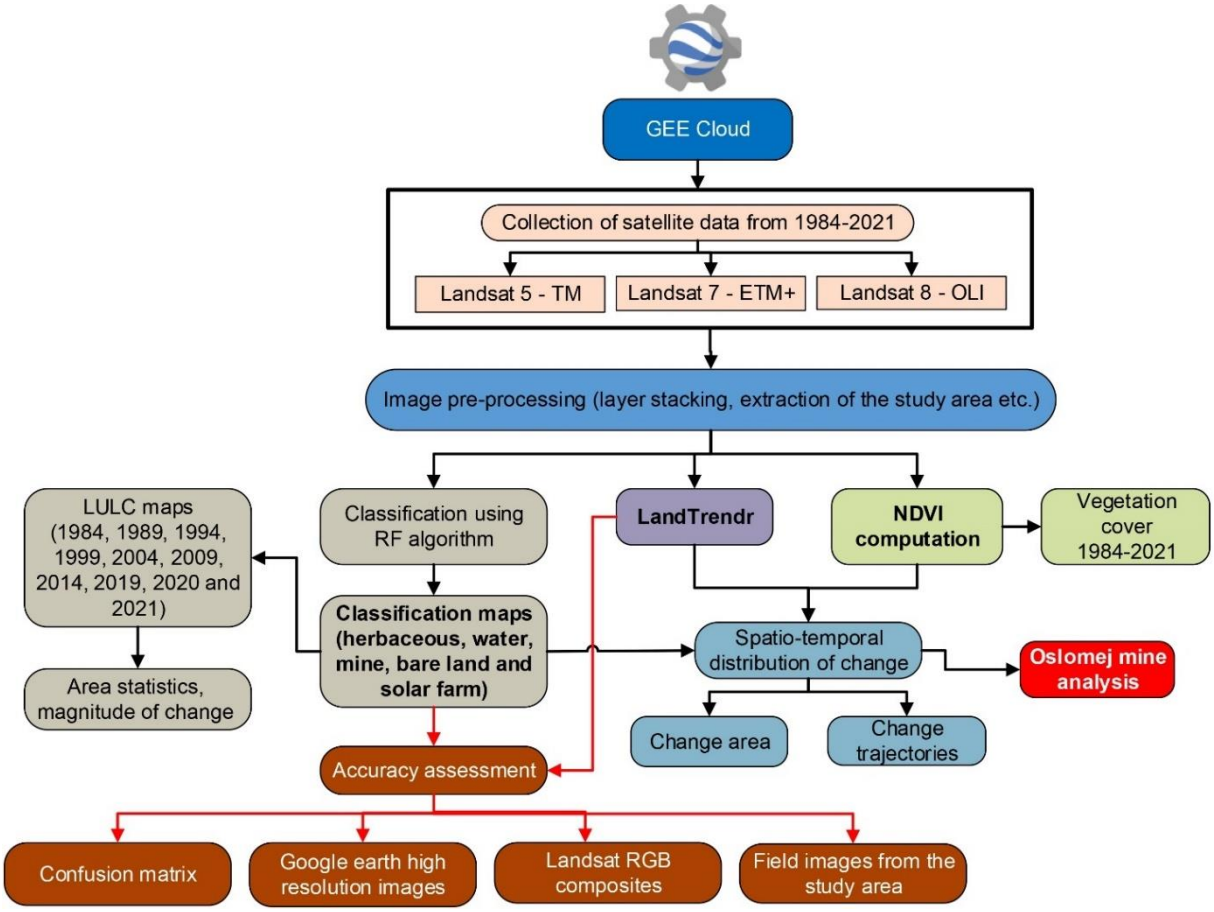

Figure 3. Overview of the research methodology

2.2.1. Monitoring of disturbance and reclamation years with LandTrendr

We employed the LandTrendr algorithm created by Kennedy et al. [36] that employs an iterative calculation that combines continuous breakpoint assessment and fitting based on the time series trajectory of a single 30 m × 30 m Landsat image pixel. The algorithm, which runs on the GEE platform, creates cloud-free mosaics from highly dense images and extracts pixel-by-pixel land surface disturbance pattern trajectories.

Each pixel's input consists of the date and an annual time series of one spectral band or index. The processing method for selecting the best model involves removing noise-induced spikes (outliers), identifying potential vertices (breakpoints), fitting trajectories, and determining the optimal number of segments. The NDVI index was used in the LandTrendr algorithm to capture the progress of vegetation restoration and disturbance caused by mining [37, 38, 39, 40]. LandTrendr calculates a collection of vertices that connect distinctive segments in NDVI time series at each pixel to identify disturbance events and patterns for deferent stages of mining.

Because mining involves the complete removal of forests, the NDVI curve drops dramatically when mining begins. The period of active mining and the duration of mining can be characterized by low NDVI values (<0.1). When mining is followed by the restoration progress, the NDVI curve steadily rises. The unaltered forested areas, whose NDVI values are typically high, are regions with no active mining operations.

2.2.2. Classification method details and accuracy assessment

RF classification algorithm with the "Classifier.randomforest" function available in the GEE library was used to classify the Landsat satellite images.

Due to its excellent performance compared to other classifiers across many datasets, RF is the most well-known ensemble learning technique for classification. It divides the data into many decision trees and predicts the class using a majority vote, while also requiring shorter training time [41].

The images were classified into five major classes – herbaceous, water, mine, bare land, and solar farm. Prior to the supervised classification of the images, the training dataset was carefully selected to provide a general pattern of the LULC classes. Classes that are incorrectly defined by the training data have an impact on the entire supervised classification process and result in incorrect classification. In order to prevent that, 100 sample points for each class were chosen and scattered around the mine's research area.

To determine classification accuracy, the sample sets were randomly divided into 70 % for training and 30 % for validation. From the resulting matrix, we derived a set of accuracy evaluation metrics extracted from the remote sensing images.

Following that, we created a confusion matrix to measure each category's overall accuracy (OA), producer accuracy (PA), user accuracy (UA) and kappa statistics (K_c) [42].

A table that shows the connection between the classification product and the reference data is called a confusion matrix. As a commission error metric, the UA indicates at what probability a pixel classified in a certain class is represented by that class on the ground. As an omission error metric, PA indicates how well training pixels of a given class are classified. To calculate the OA, the sum of correctly classified pixels was divided by the total number of sampled pixels. The equations used are as follows [42]:

$$PA = \frac{n_{ii}}{n_{icol}} \tag{2}$$

$$UA = \frac{n_{ii}}{n_{irow}} \tag{3}$$

$$OA = \frac{1}{N}\sum_{i=1}^{r} n_{ii} \tag{4}$$

$$K_c = \sum_{i=1}^{r} n_{ii} - \sum_{i=1}^{r} \frac{n_{icol}n_{irow}}{N^2} - \sum_{i=1}^{r} n_{icol}n_{irow} \tag{5}$$

where r denotes the number of rows, n_{ii} is the number of pixels that were correctly classified in a given class, n_{icol} is the column (reference data) and n_{irow} is the row (predicted classes) total, and N is the total number of pixels in the confusion matrix.

2.3. Change detection

The changes in the classes between 1984 and 2021 were determined using the LULC classification results. The net change and percent change of the LULC classes between the years 1984 and 1989, 1989 and 1994, 1994 and 1999, 1999 and 2004, 2004 and 2009, 2009 and 2014, 2014 and 2019, 2019 and 2020, and 2020 and 2021 were calculated using the LULC area distribution results.

To calculate the percentage change (%), present and previous LULC areal extent were compared using the following formula:

$$\text{Percentage change (\%)} = \frac{\text{LULC area (present)} - \text{LULC area (previous)}}{\text{LULC area (previous)}} * 100 \quad (6)$$

3. Results and discussion

3.1. Spatio-temporal progression of mine-induced disturbance and restoration over Oslomej mine between 1984-2021

Oslomej mine with an annual production of 1.2 x 10^6 t of coal started operating in 1980. This deposit is divided into two areas with the river Temnica, as follows:

- "Oslomej-East", with exploitation from 1980-2007.
- "Oslomej-West" with exploitation from 2007-2019.

The coal mining in "Oslomej – West" is a continuation of the exploitation after the completion of the activities in "Oslomej – East". In order to maintain that continuity, the river Temnica was dislocated with the construction of a regulated riverbed, which now passes in the area of the used mine "Oslomej-East".

High temporal detail analyses of the mining and restoration patterns over the Oslomej mine site have been done for the first time.

Figure 4 shows the chronological variability of NDVI that represent activities related to mining and restoration over the Oslomej mine between 1984 and 2021.

Although exploitation at the Oslomej mine began in 1980, our analysis starts in 1984 because that is the starting operation year for the Landsat 5 satellite.

We chose not to select data for 2012 to avoid the impact of the missing scan line data in Enhanced Thematic Mapper (ETC) images, which was present due to the scan line corrector failure of Landsat 7.

The images from 1984 to 2021 or 36 years (excluding the year 2012) of coverage were all put through the workflow that we previously explained in order to create the mine time series.

We started this analysis in the year 1984 to observe progressions of the mining activities in the "Oslomej-East" area of the open-pit mine.

From 1984 to 1990, the appearance of considerable mining activities was notable, with reduced NDVI values that were noticeable over the northern part of the "Oslomej-East" area of the open-pit mine (Figure 4).

From 1991 to 2000, the continuous decline of NDVI signified progressions of mining activities that are slowly shifting south in the "Oslomej-East" area. During this period, slight changes in the positive direction of NDVI values are noticed in the northern part of the "Oslomej-East" area, which marks the beginning of the reclamation of this previously excavated part.

From 2001 to 2006, the exploitation of the central part of the mine is evident, with the start of preparatory work for the opening the "Oslomej-West" area of the open-pit mine.

2007-2008, mark the beginning of the exploitation in the "Oslomej-West" area which is evident by the reduced NDVI values of the northern part of the mine.

From 2009 to 2018, there is a progression of the mine to the south in the "Oslomej-West" area. What we can notice from the analysis of this period is that in parallel with the progression of the mine, the reclamation of the previously excavated parts begins, which is proven by the NDVI values greater than 0.4. Also, the formation of Lake Oslomej is evident in the southern part of the "Oslomej-West" area, after the year 2013 (Figure 4, Figure 10).

The year 2019 marks the end of exploitation in the "Oslomej-West" area of the open-pit mine. From the analysis made for the year 2019, it can be concluded that "Oslomej-East" area is completely reclaimed which is evident by the high NDVI values (in some cases greater than 0.6). Also from the analyses, high values of NDVI are noticed in the northern part of the "Oslomej-West" area, which means that this part also has been successfully reclaimed.

In 2020, no major disturbances were recorded in the NDVI values, which means that there are no major activities in the mine area.

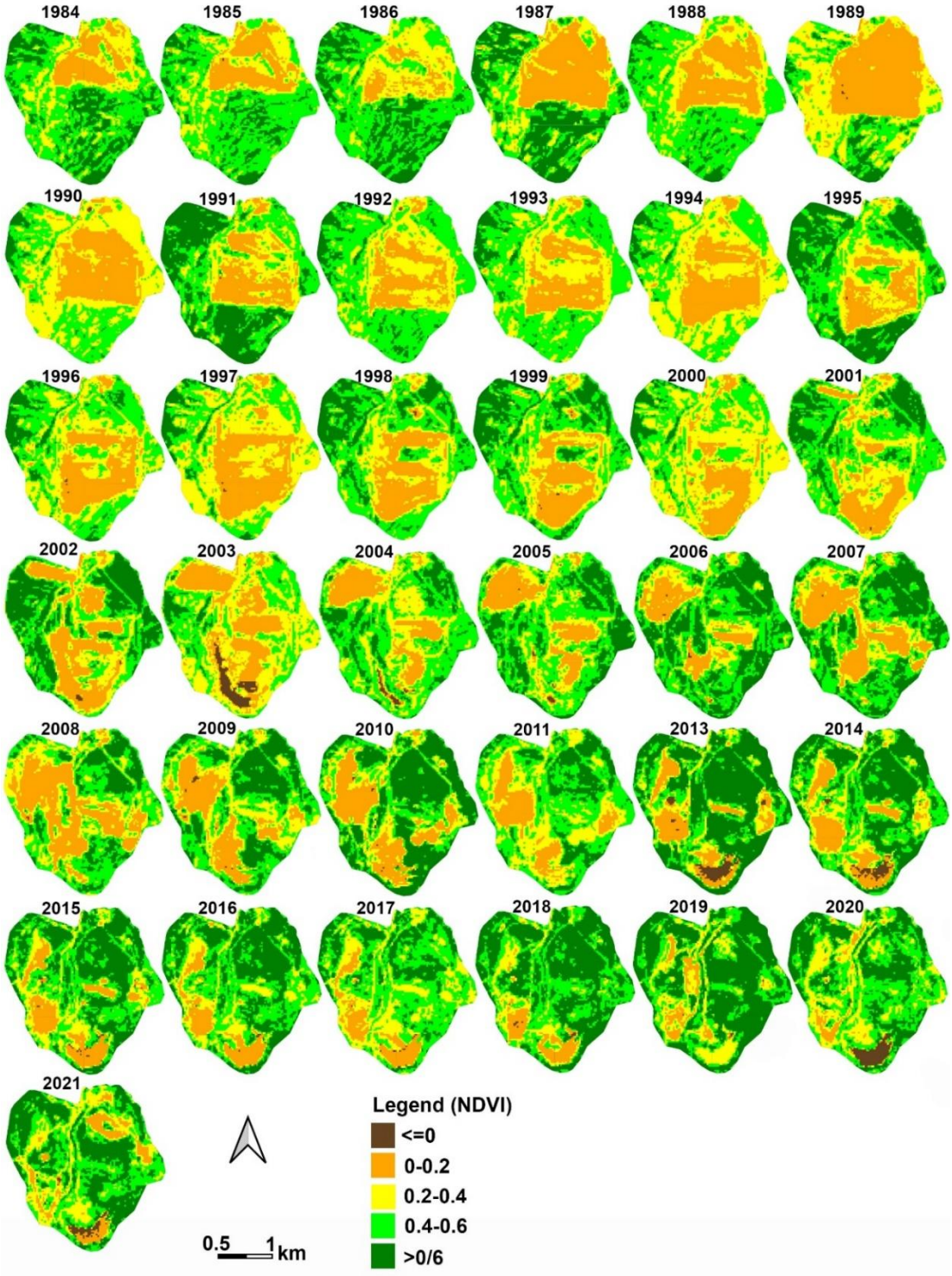

Figure 4. Spatio-temporal variability of NDVI over the Oslomej mine for the period from 1984 to 2021

The year 2021 marks the beginnings of the implementation of the project for photovoltaic power plants in the area of the former open-pit mine "Oslomej". The project was developed in accordance with the Energy Development Strategy of the Government of R. N. Macedonia, based on the European Green Agreement, to transform the production of electricity and increase the use of renewable energy sources at the expense of fossil fuels. The 10 MW "Oslomej 1" photovoltaic power plant is the first example of an energy transition in Southeast Europe in which electricity will be generated from the sun through panels placed on an old, depleted coal mine. The goal of this project is the construction of two more solar farms (Oslomej 2 and 3) in the area of the former coal mine with a total installed capacity of 120 MW. From the analysis made for year 2021, it is evident the preparatory work followed by low values of NDVI in the northern part of the "Oslomej-East", which indicates the construction activities related to the construction of this solar farm ("Oslomej 1").

Figure 5 shows the time series analysis for the year 2021, in which is clearly evident the construction of the solar farm.

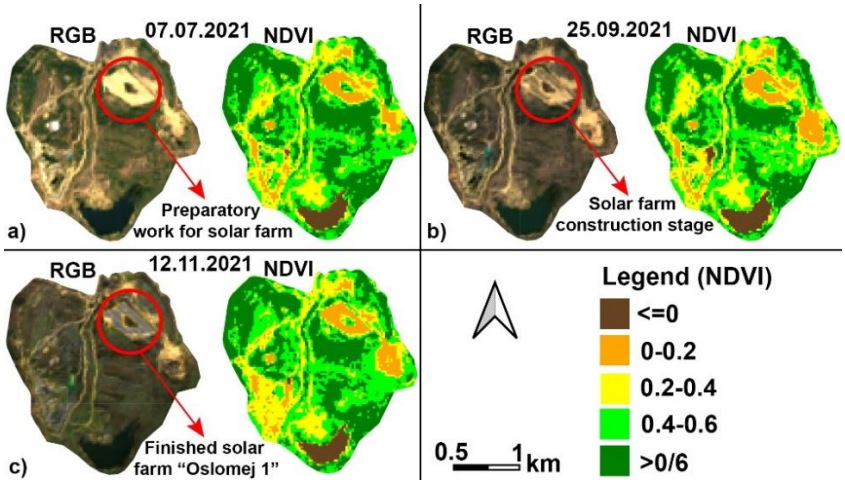

Figure 5. Landsat imagery and NDVI maps of the study area showing the construction of the solar farm in 2021

From Figure 5 can be concluded that the preparatory works and the construction process of the solar farm are clearly visible from the RGB compositions, while in the NDVI compositions there is a noticeable low value (0-0.2) which indicates a lack of vegetation. In order to be able to clearly distinguish the area on which the photovoltaic panels are installed, it is necessary to make an additional classification with RF classification algorithm.

3.2. Spatio-temporal dynamics profile of disturbance and recovery at different sites over the Oslomej mine

By carefully analysing the entire NDVI time-series pattern at several sites over the Oslomej Mine using the LandTrendr algorithm, we enhanced the above analysis to provide a thorough picture of the disturbance and recovery dynamics from 1984 to 2021. Four sites in the active mining area had their unique pixel trajectories analysed. The spatio-temporal NDVI mapping of the mining disturbance and reclamation years for the four site-specific pixels with a resolution of 30x30 m are shown in Figures 6-9. Besides the spatiotemporal NDVI mapping shown on the figures, we also included a high-resolution Google Earth image and RGB Landsat composites of selected years for visual analyses.

From Figure 6, it is clear that exploitation in site 1 which is located in the northern part of the "Oslomej-East" area started before 1984. As would be expected, lower NDVI values (<0.2) are noticeable throughout the mining operation until a substantial increase of NDVI values (>0.4) in 1998 when the rehabilitation began. High NDVI values that are equated with the reclamation process are observed until 2019 when the land preparatory and construction activities related to solar farm "Oslomej 1" began.

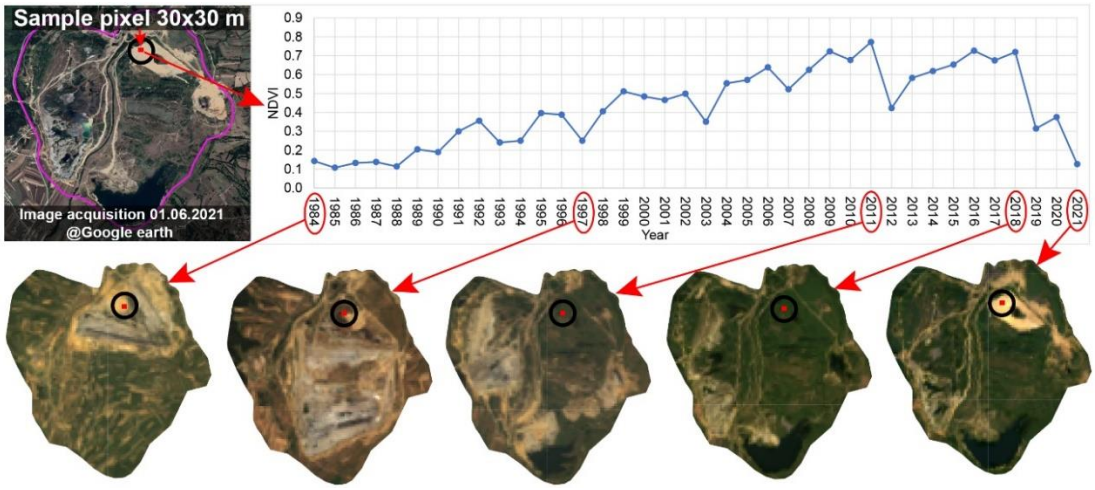

Figure 6. True colour images and temporal NDVI trajectory for site 1 (spectral values for the pixel 30 x 30 m) for the period 1984 to 2021. Lower NDVI values indicate mining, while higher values represent vegetation

Mining operations at site 2 which is in the southern part of the “Oslomej-East” area began in 1994 as evidenced by decline in the NDVI signal shown in Figure 7. Mining activities are present in this area from 1994 to 2005. After 2005 we have a slight increase in NDVI values that indicate that the reclamation process has begun. In 2021 the area is completely reclaimed which can be seen from the RGB Landsat composite as well as the high NDVI value (>0.45) related to the location.

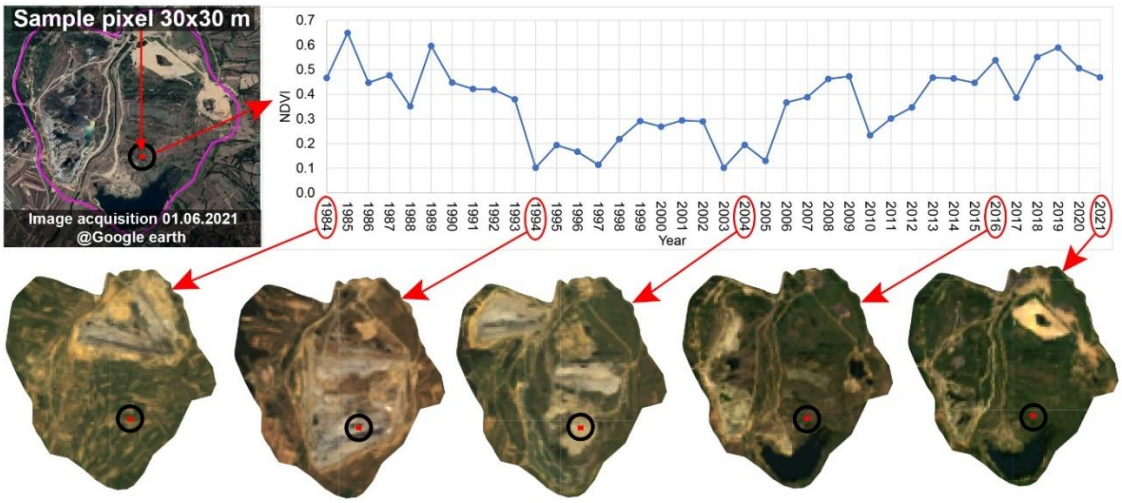

Figure 7. True colour images and temporal NDVI trajectory for site 2 (spectral values for the pixel 30 x 30 m) for the period 1984 to 2021. Lower NDVI values indicate mining, while higher values represent vegetation

On Site 3, which is situated in the northern portion of the "Oslomej-West" region, there have been brief disturbances in the past (1984-2002) shown in Figure 8. These could be caused by anthropogenic and natural factors but are definitely not from mining. From 2003 to 2014, mining activities at Site 3 clearly showed a disruption pattern, with the NDVI declining from ~0.5 to 0.15 and remaining low until 2014, when a significant recovery from 2015-2016 to 0.5 occurred, indicating the start of the reclamation process. The high NDVI values that are followed in the coming years until 2021 indicate a fully reclaimed area.

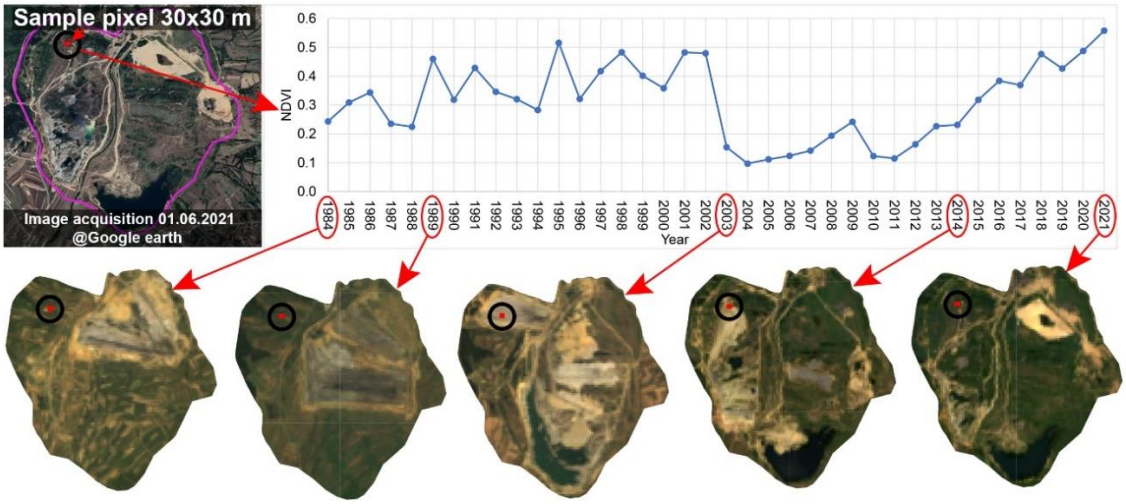

Figure 8. True colour images and temporal NDVI trajectory for site 3 (spectral values for the pixel 30 x 30 m) for the period 1984 to 2021. Lower NDVI values indicate mining, while higher values represent vegetation

Site 4 in the southern portion of the "Oslomej-West" area (Figure 9) displayed an NDVI pattern that was relatively consistent from 1984 to 2012 with a small but discernible decline in 1988. As can be seen from Figure 9, the tendency of NDVI to form a U-shaped pattern from 2012 to 2021 is apparent. In both the pre-and post-mining phases of its lifespan, higher NDVI values are predominant, with the lowest values occurring at the culmination of the mining activities from 2013 to 2018. The increase in NDVI from 0.11 in 2018 to 0.41 in 2021 shows that rehabilitation started as soon as mining activities were completed (Figure 9).

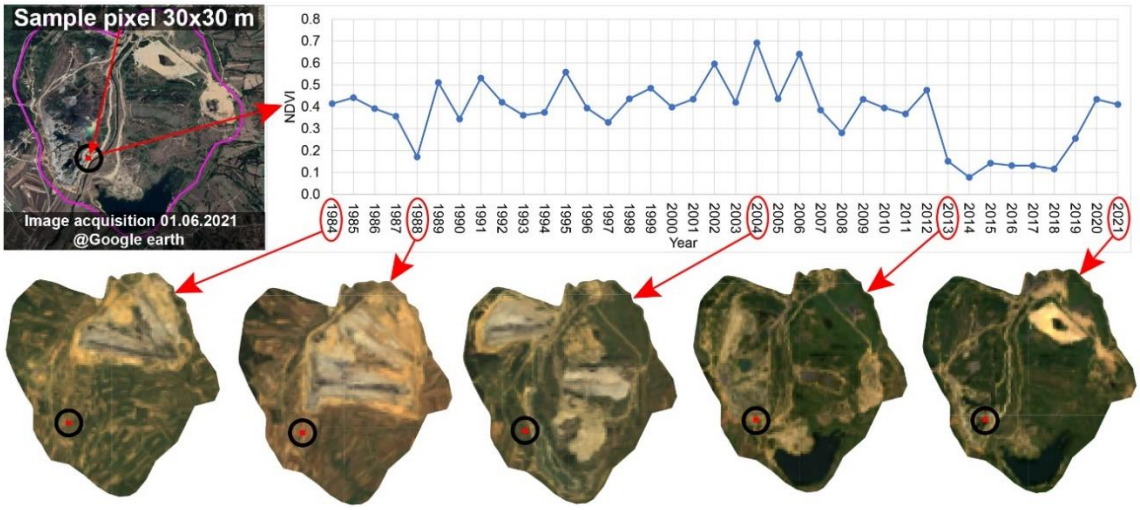

Figure 9. True colour images and temporal NDVI trajectory for site 4 (spectral values for the pixel 30 x 30 m) for the period 1984 to 2021. Lower NDVI values indicate mining, while higher values represent vegetation

3.3. Assessment of areal extent and change of LULC

LULC maps for the years 1984, 1989, 1994, 1999, 2004, 2009, 2014, 2019, 2020 and 2021 were produced after editing and finalization. In the study region, there were five main types of land cover identified: herbaceous, water, mine, bare land, and solar farm. The areas of each class in hectares were extracted and used for statistical analysis. Figure 10 shows the LULC maps of the research area for ten distinct time periods.

Spatial distribution and area statistics with the percentages of the area covered by each LULC categories are shown in Table 1. The magnitude of change for each LULC category over a 5-year time span from 1984 to 2021 is depicted in Table 2.

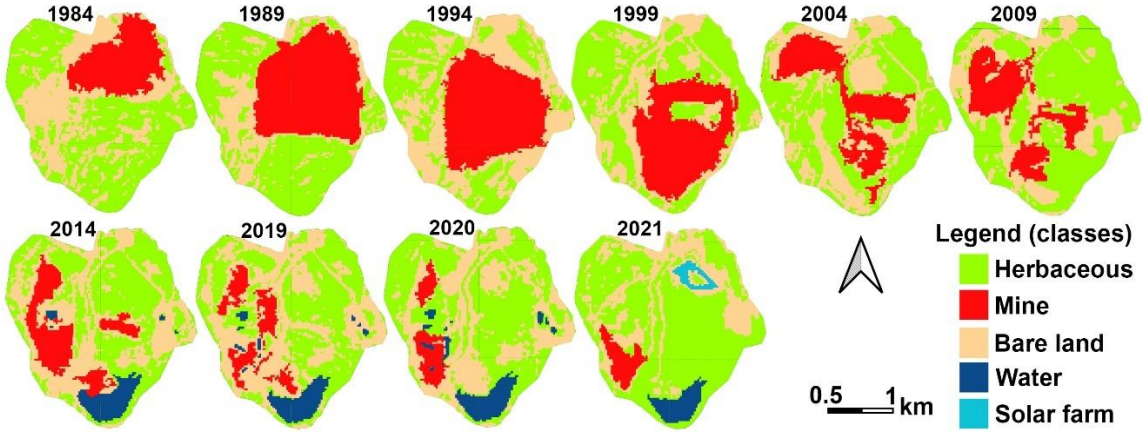

Figure 10. The maps depicting the LULC changes in the Oslomej coal field area for ten different time periods from 1984 to 2021

Table 1. LULC classes areal distribution across the Oslomej coal mine (expressed in hectares; percentages are indicated by values in parenthesis)

LULC classes	1984	1989	1994	1999	2004	2009	2014	2019	2020	2021
Herbaceous	301.3 (47.6)	275.8 (43.6)	183.4 (29.0)	283.1 (44.7)	299.7 (47.3)	362.3 (57.2)	274.4 (43.3)	265.7 (42.0)	322.2 (50.9)	392.5 (62.0)
Mine	143.1 (22.6)	224.3 (35.4)	238.1 (37.6)	204.4 (32.3)	139.2 (22.0)	126.5 (20.0)	92.4 (14.6)	67.63 (10.7)	53.3 (8.4)	48.2 (7.6)
Bare land	188.6 (29.8)	132.9 (21.0)	211.5 (33.4)	145.6 (23.0)	194.1 (30.7)	144.3 (22.8)	225 (35.5)	256.7 (40.6)	209.9 (33.2)	148.5 (23.5)
Water	0 (0)	0 (0)	0 (0)	0 (0)	0 (0)	0 (0)	41.18 (6.5)	43 (6.8)	47.7 (7.5)	31.7 (5.0)
Solar farm	0 (0)	0 (0)	0 (0)	0 (0)	0 (0)	0 (0)	0 (0)	0 (0)	0 (0)	11.9 (1.9)

Table 2. Net change in areal extent of LULC classes
(expressed in hectares; percentages are indicated by values in parenthesis).

LULC classes	1984-1989	1989-1994	1994-1999	1999-2004	2004-2009	2009-2014	2014-2019	2019-2020	2020-2021
Herbaceous	-25.5 (-8.5)	-92.4 (-33.5)	99.7 (54.4)	16.6 (5.9)	62.6 (20.9)	-87.9 (-24.3)	-8.7 (-3.2)	56.5 (21.3)	70.3 (21.8)
Mine	81.2 (56.7)	13.8 (6.2)	-33.7 (-14.2)	-65.2 (-31.9)	-12.7 (-9.1)	-34.1 (-27.0)	-24.77 (-26.8)	-14.33 (-21.2)	-5.1 (-9.6)
Bare land	-55.7 (-29.5)	78.6 (59.1)	-65.9 (-31.2)	48.5 (33.3)	-49.8 (-25.7)	80.7 (55.9)	31.7 (14.1)	-46.8 (-18.2)	-61.4 (-29.3)
Water	0 (0)	0 (0)	0 (0)	0 (0)	0 (0)	41.18 (/)	1.82 (4.4)	4.7 (10.9)	-16 (-33.5)
Solar farm	0 (0)	0 (0)	0 (0)	0 (0)	0 (0)	0 (0)	0 (0)	0 (0)	11.9 (/)

It is observed that the herbaceous cover has decreased from 301.3 hectares (47.6 %) in the year 1984 to 275.8 hectares (43.6 %) in the year 1989, and further decreased to 183.4 hectares (29 %) by the year 1994. The decrease in the herbaceous cover is due to the expansion of the mine pits. The herbaceous cover was 283.1 hectares (44.7 %) in the year 1999, which gradually increased to 299.7 hectares (47.3 %), 362.3 hectares (57.2 %), in the year 2004, 2009 respectively. It again decreases to 274.4 hectares (43.3 %) in the year 2014 and 265.7 hectares (42.0 %) in the year 2019. The years 2020 and 2021 show an increase from 322.2 hectares (50.9 %) to 392.5 hectares (62.0) showing a net increase of 70.3 hectares (21.8 %) (Tables 1 and 2).

The coal mining area in the Oslomej mine that had spread over 143.1 hectares (22.6 %) in 1984, increased to 224.3 hectares (35.4 %) in 1989 and again it increased to 238.1 hectares (37.6) in the year 1994. The mine cover was 204.4 hectares (32.3 %) in the year 1999 which gradually decreased to 139.2 hectares (22 %), 126.5 hectares (20.0 %), 92.4 hectares (14.6 %), 67.63 hectares (10.7 %), 53.3 hectares (8.4 %), 48.2 hectares (7.6 %), in the year 2004, 2009, 2014, 2019, 2020, 2021 respectively.

The land cover category of barren land decreased from 188.6 hectares (29.8 %) in the year 1984 to 132.9 hectares (21 %) in the year 1989. However, barren land increased to 211.5 hectares (33.4 %) in the year 1994 which gradually decreased to 145.6 hectares (23 %) in 1999. In the following periods we have a slight increase and decrease of the barren land as follows: 194.1 hectares (30.7 %) in 2004, decrease to 144.3 hectares (22.8 %) in 2009, increased to 225 hectares (35.5 %) in 2014, and 256.7 hectares (40.6 %) in 2019, slightly decreased to 209.9 hectares (33.2 %) in 2020 and further decreased to 148.5 hectares (23.5 %) in 2021.

The water body of the study area appears in 2014 and shows a fairly stable trend covering an area of 41.18 hectares (6.5 %) and 43 hectares (6.8 %) in the year 2014 and 2019 respectively. However, the total area of the water body for a duration of one year has decreased from 47.7 hectares (7.5 %) in the year 2020 to 31.7 hectares (5 %) in the year 2021 showing a net decrease of -16 hectares (-33.5 %) (Tables 1 and 2).

The land cover category of solar farm appears in 2021 with an area of 11.9 hectares (1.9 %) which means that in this period is constructed the solar farm “Oslomej 1” with an installed capacity of 10 MW.

3.4. Accuracy Assessment

3.4.1. Accuracy Assessment for Initial Classification

We now examine the degree to what extent our classification method distinguished the LULC classes within the Oslomej mine site. The average UA of the classified images of 1984, 1989, 1994, 1999, 2004, 2009, 2014, 2019, 2020 and 2021 were found to be 0.95, 0.92, 0.96, 0.87, 0.9, 0.89, 0.9, 0.9, 0.88 and 0.89 respectively (Figure 11). The average PA of the classified images of 1984, 1989, 1994, 1999, 2004, 2009, 2014, 2019, 2020 and 2021 were found to be 0.95, 0.91, 0.95, 0.86, 0.9, 0.89, 0.9, 0.9, 0.88 and 0.86 respectively (Figure 11). Overall classification accuracy for the analysed classified images from the years 1984, 1989, 1994, 1999, 2004, 2009, 2014, 2019, 2020 and 2021 were found to be 0.95, 0.92, 0.96, 0.88, 0.9, 0.9, 0.9, 0.9, 0.9 and 0.86, respectively, whereas the kappa statistics for the classed images from the same years were 0.93, 0.88, 0.94, 0.82, 0.86, 0.85, 0.87, 0.87, 0.86, 0.82, respectively (Figure 11). These accuracy levels are acceptable and comparable with related studies [43, 44, 45].

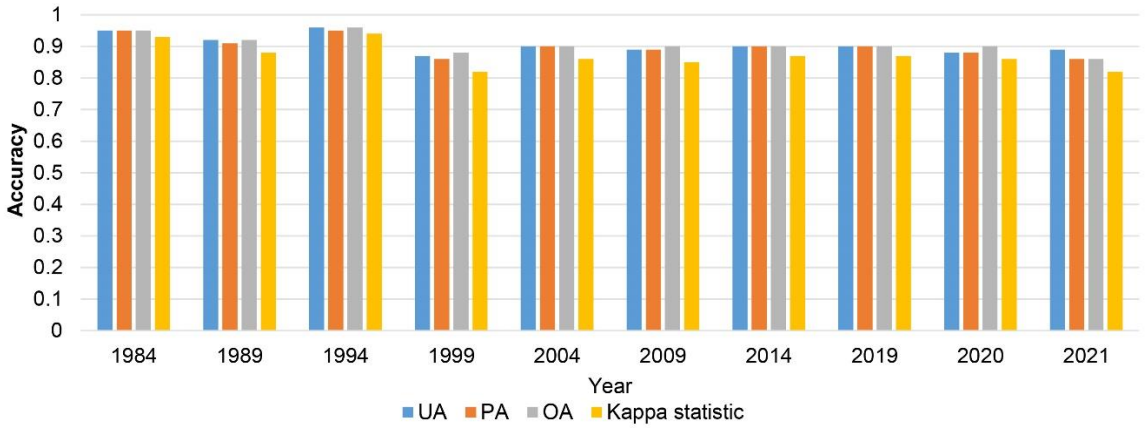

Figure 11. Overview of accuracy assessment for initial classification for selected years

Each of the maps created by this classification was compared to the ground reference data by taking into account the random sample points, field knowledge, imagery, and Google Earth in order to evaluate the accuracy of the classification findings. Figure 12 shows these comparative results only for the year 2021.

Figure 12. Field comparison of the classification results. a) Classification map of the research area for 12.11.2021. b) Google Earth image form the study area for 01.11.2021 c) Field images from the solar farm "Oslomej 1". d) Field images from the Oslomej Lake

3.4.2. Accuracy Assessment for LandTrendr

Overall, the LandTrendr algorithm seems to be a useful tool for gathering data on the dynamics of historical disturbance and recovery at surface mining sites. Aside from disruptions brought on by mining activities, LandTrendr can capture partial disturbances associated with anthropogenic factors and drought stress.

The spectral signal may be impacted by a wide range of factors; thus, validation is necessary to determine the causes of any decline in NDVI values.

The images themselves are the most trustworthy source for assessment when there are no independent validation data available.

In our case, Google Earth historical imagery and Landsat RGB composites served as a crucial aid for interpreting the land cover.

Because of the contrast between the brighter patches suggesting active mining and the forested areas, the disturbance years linked with the mined "bare" areas on Google Earth high-resolution images and the Landsat RGB composites were easily distinguished.

This validation process was performed and repeated at each of the four mine locations over the study period. Where the Google Earth high-resolution images were not available, we used the Landsat RGB composites.

We visually interpreted each of the site-specific pixels by superimposing the images with the LandTrendr map in the Qgis environment. We determined whether the chosen sites had been rehabilitated after mining activities by methodically scrutinizing the images. This helped to separate mine-related disturbances from those caused by other activities.

Following this step, we compare the trajectory analysis by inspecting the Landsat NDVI composites (Figure 4) along with the NDVI time-series pattern for the chosen mine site-specific pixels (Figure 6-9). The accuracy of an analysis is determined by how closely the result compares to the reference data (high-resolution imagery from Google Earth, NDVI composites, and RGB composites from Landsat).

Our validation results demonstrate that the year of disturbance and recovery detection provided by Landtrendr algorithm is comparable to the time of detection in Google Earth high-resolution imagery, Landsat NDVI composites and Landsat RGB composites as can be seen from Figures (4, 6-9 and 12).

4. Conclusions

In this study, we examined the annual change in the Oslomej coal mine in R. N. Macedonia using long time-series data from the Landsat archive. An effective method based on an NDVI, RF classification, and LandTrendr algorithm was used to obtain a 36-year annual monitoring result from 1984 to 2021 in a surface coal mining area.

The objective of this study is to use the multiple-year NDVI to track changes in the mining area and the variation of restoration vegetation at the Oslomej coal mine. Our findings show decreasing NDVI trend around mining activities, followed by an increase that coincided with the end of exploitation and the apparent efforts at restoration in the mining area.

Five major LULC classes labelled as herbaceous, water, mine, bare land and solar farm have been clearly identified from the Oslomej coal mining area. The RF classification algorithm was capable of separating the LULC classes within the affected area with accuracies exceeding 90 %. The study also provides the spatial distribution, area statistics and the magnitude of change in different LULC categories during the time period from 1984 to 2021.

The LandTrendr trajectory analysis clearly identified patterns of mine disturbance over the course of the research period, the duration of active mining, and the progress of restoration.

We demonstrate that the methodology presented in this study executed through GEE can efficiently and precisely determine the annual extent of surface mining, restoration vegetation status and solar farm growth in the selected study area.

This study attempted to offer an effective methodology for the mining authorities and the institutions from the government to get inexpensive information that is easily accessible for characterizing and monitoring the disturbance and recovery patterns in mining regions. Additionally, this study also offers data support and analyses for mining development supervision and environmental protection. We also provide a foundation for further research on significant ecological disturbances. Remote sensing images can be used to observe phenomena such as urbanization, forest loss, agriculture, or changes in land areas, and analyses such as the one we describe here show how simple it is to identify the trends behind those big data.

Our results and discussions point to the fact that there are positive examples of successful vegetation restoration and transformation of mining areas into solar farms such as the example with the former Oslomej mine.

The presented methodology in this study is fairly adaptable because it may be used to analyze various situations of land surface change and should yield equally trustworthy results. Additionally, it is easily adaptable to various regions, such as those in countries with limited resources.

References

[1] **Farjana, S.H., N. Huda, M.A. Parvez Mahmud, and R. Saidur.,** 2019
A review on the impact of mining and mineral processing industries through life cycle assessment, Journal of Cleaner Production, Vol. 231, 1200-1217. DOI: https://doi.org/10.1016/j.jclepro.2019.05.264.

[2] **Tost, M., M. Hitch, V. Chandurkar, P. Moser, and S. Feiel.,** 2018
The state of environmental sustainability considerations in mining, Journal of Cleaner Production, Vol. 182, 969-977. DOI: https://doi.org/10.1016/j.jclepro.2018.02.051.

[3] **Norgate, T. and N. Haque.,** 2010
Energy and greenhouse gas impacts of mining and mineral processing operations, Journal of Cleaner Production, Vol. 18, No. 3, 266-274. DOI: https://doi.org/10.1016/j.jclepro.2009.09.020.

[4] **Hilson, G., and V. Nayee.,** 2002
Environmental management system implementation in the mining industry: a key to achieving cleaner production, International Journal of Mineral Processing, Vol. 64, No.1, 19-41. DOI: https://doi.org/10.1016/S0301-7516(01)00071-0

[5] **Hilson, G.,** 2003
Defining "cleaner production" and "pollution prevention" in the mining context, Minerals Engineering, Vol. 16, No. 4, 305-321. DOI: https://doi.org/10.1016/S0892-6875(03)00012-8.

[6] **Islam, K., R. Yokoi., M. Motoshita., and S. Murakami.,** 2022
Ecological footprint accounting of mining areas and metal production of the world, Resources, Conservation and Recycling, Vol. 183, 106384. DOI: https://doi.org/10.1016/j.resconrec.2022.106384.

[7] **Watari, T., K. Nansai., and K. Nakajima,** 2021
Major metals demand, supply, and environmental impacts to 2100: A critical review, Resources, Conservation and Recycling, Vol. 164, 105107. DOI: https://doi.org/10.1016/j.resconrec.2020.105107.

[8] **Werner, T.T., G.M. Mudd., A.M. Schipper., M.A.J. Huijbregts., L. Taneja., and S.A. Northey.,** 2020
Global-scale remote sensing of mine areas and analysis of factors explaining their extent, Global Environmental Change, Vol. 60, 102007. DOI: https://doi.org/10.1016/j.gloenvcha.2019.102007.

[9] **Li, Q., J. Guo., F. Wang., and Z. Song.,** 2021
Monitoring the Characteristics of Ecological Cumulative Effect Due to Mining Disturbance Utilizing Remote Sensing, Remote Sensing, Vol. 13, No. 24, 5034. DOI: https://doi.org/10.3390/rs13245034

[10] **Nascimento, F.S., M. Gastauer., P.W.M. Souza-Filho., W.R. Nascimento., D.C. Santos., M.F. Costa.,** 2020
Land Cover Changes in Open-Cast Mining Complexes Based on High-Resolution Remote Sensing Data, Remote Sensing, Vol. 12, No. 4, 611. DOI: https://doi.org/10.3390/rs12040611

[11] **Padmanaban, R., A.K. Bhowmik., and P. Cabral.,** 2017
A Remote Sensing Approach to Environmental Monitoring in a Reclaimed Mine Area, ISPRS International Journal of Geo-Information, Vol. 6, No.12, 401. DOI: https://doi.org/10.3390/ijgi6120401

[12] **Chen, W., X. Li., H. He., and L. Wang.,** 2018
A Review of Fine-Scale Land Use and Land Cover Classification in Open-Pit Mining Areas by Remote Sensing Techniques, Remote Sensing, Vol.10, No.1, 15. DOI: https://doi.org/10.3390/rs10010015

[13] **Townsend, P.A., D.P. Helmers., C.C. Kingdon., B.E. McNeil., K.M. de Beurs., and K.N. Eshleman.,** 2009
Changes in the extent of surface mining and reclamation in the Central Appalachians detected using a 1976–2006 Landsat time series, Remote Sensing of Environment, Vol. 113, No. 1, 62-72. DOI: https://doi.org/10.1016/j.rse.2008.08.012.

[14] **Zhang, Z., G. He., M. Wang., Z. Wang., T. Long., and Y. Peng.,** 2015
Detecting Decadal Land Cover Changes in Mining Regions based on Satellite Remotely Sensed Imagery: A Case Study of the Stone Mining Area in Luoyuan County, SE China, Photogrammetric Engineering & Remote Sensing, (2015), Vol. 81, No. 9, 745-751. DOI: https://doi.org/10.14358/PERS.81.9.745.

[15] **Guan, C., B. Zhang., J. Li., and J. Zhao.,** 2017
Temporal and spatial changes of land use and landscape in a coal mining area in Xilingol grassland, IOP Conference Series: Earth and Environmental Science, Vol.52, 12052. DOI: 10.1088/1742-6596/52/1/012052.

[16] **Alkan, M., M. Oruc., Y. Yildirim., D.Z. Seker., and K. Jacobsen.,** 2013
Monitoring Spatial and Temporal Land Use/Cover Changes; a Case Study in Western Black Sea Region of Turkey, Journal of the Indian Society of Remote Sensing, Vol. 41, No.3, 587-596. DOI: 10.1007/s12524-012-0227-2.

[17] **Zhao, H., Y. Ma., F. Chen., J. Liu., L. Jiang., W. Yao., and J. Yang.,** 2018
Monitoring Quarry Area with Landsat Long Time-Series for Socioeconomic Study, Remote Sensing, Vol.10, No.4, 517. DOI: https://doi.org/10.3390/rs10040517

[18] **Dorren, L.K.A., B. Maier., and A.C. Seijmonsbergen.,** 2003
Improved Landsat-based forest mapping in steep mountainous terrain using object-based classification, Forest Ecology and Management, Vol. 183, No.1, 31-46. DOI: https://doi.org/10.1016/S0378-1127(03)00113-0.

[19] **Hansen, M.C., P. Potapov., R. Moore., M. Hancher., S. Turubanova., A. Tyukavina., D. Thau., S. Stehman., S. Goetz., T. Loveland., A. Kommareddy., A. Egorov., L. Chini., C.O. Justice., and J. Townshend.,** 2013
High-Resolution Global Maps of 21st-Century Forest Cover Change, Science (New York, N.Y.), Vol. 342, 850-853 DOI: 10.1126/science.1244693.

[20] **Kennedy, R.E., W.B. Cohen., and T.A. Schroeder.,** 2007
Trajectory-based change detection for automated characterization of forest disturbance dynamics, Remote Sensing of Environment, Vol. 110, No.3, 370-386 DOI: https://doi.org/10.1016/j.rse.2007.03.010.

[21] **Li, J., L.P. Jiao., Y.Y. Shen., and Q.L. Liu.,** 2016
Land use and cover change in coal mining area by IFZ and NDVI, Vol. 41, 2822-2829. DOI: 10.13225/j.cnki.jccs.2016.0223.

[22] **Li, J., Yan, X., Yang, Z., Dong, J., Deng, X.,** 2019
Comparative analysis of long-term trends on fraction of vegetation coverage in grassland mining area, Bulletin of Surveying and Mapping, Vol. 8, 130-134. DOI: 10.13474/j.cnki.11-2246.2019.0267.

[23] **Xiao, W., X. Deng., T. He., and W. Chen.,** 2020
Mapping Annual Land Disturbance and Reclamation in a Surface Coal Mining Region Using Google Earth Engine and the LandTrendr Algorithm: A Case Study of the Shengli Coalfield in Inner Mongolia, China, Remote Sensing, (2020), Vol. 12, No. 10, 1612. DOI: https://doi.org/10.3390/rs12101612

[24] **He, T., W. Xiao., Y. Zhao., W. Chen., X. Deng., and J. Zhang.,** 2021
Continues monitoring of subsidence water in mining area from the eastern plain in China from 1986 to 2018 using Landsat imagery and Google Earth Engine, Journal of Cleaner Production, Vol. 279, 123610. DOI: https://doi.org/10.1016/j.jclepro.2020.123610.

[25] **Bao, N.-s., L.-x. Wu., S.-j. Liu., and N. Li.,** 2016
Scale parameter optimization through high-resolution imagery to support mine rehabilitated vegetation classification, Ecological Engineering, Vol. 97, 130-137. DOI: https://doi.org/10.1016/j.ecoleng.2016.06.117.

[26] **Wanat, N., E. Joussein., M. Soubrand., and J.F. Lenain.,** 2014
Arsenic (As), antimony (Sb), and lead (Pb) availability from Au-mine Technosols: a case study of transfer to natural vegetation cover in temperate climates, Environ Geochem Health, Vol. 36, No. 4, 783-795. DOI: 10.1007/s10653-014-9596-5.

[27] **Gorelick, N., M. Hancher., M. Dixon., S. Ilyushchenko., D. Thau., and R. Moore.,** 2017
Google Earth Engine: Planetary-scale geospatial analysis for everyone, Remote Sensing of Environment, (2017), Vol. 202, 18-27. DOI: https://doi.org/10.1016/j.rse.2017.06.031.

[28] **Yi, Z., M. Liu., X. Liu., Y. Wang., L. Wu., Z. Wang., and L. Zhu.,** 2021
Long-term Landsat monitoring of mining subsidence based on spatiotemporal variations in soil moisture: A case study of Shanxi Province, China, International Journal of Applied Earth Observation and Geoinformation, Vol. 102, 102447. DOI: https://doi.org/10.1016/j.jag.2021.102447.

[29] **Dlamini, L.Z.D. and S. Xulu.,** 2019
Monitoring Mining Disturbance and Restoration over RBM Site in South Africa Using LandTrendr Algorithm and Landsat Data, Sustainability, Vol. 11, No. 24, 6916.

[30] **Zhang, M., T. He., G. Li., W. Xiao., H. Song., D. Lu., and C. Wu.,** 2021
Continuous Detection of Surface-Mining Footprint in Copper Mine Using Google Earth Engine, Remote Sensing, Vol. 13, No. 21, 4273. DOI: https://doi.org/10.3390/rs13214273

[31] **Li, J., Z. Jiang., H. Miao., J. Liang., Z. Yang., Y. Zhang., and T. Ma.,** 2022
Identification of cultivated land change trajectory and analysis of its process characteristics using time-series Landsat images: A study in the overlapping areas of crop and mineral production in Yanzhou City, China, Science of The Total Environment, Vol. 806, 150318. DOI: https://doi.org/10.1016/j.scitotenv.2021.150318.

[32] **Pericak, A.A., C.J. Thomas., D.A. Kroodsma., M.F. Wasson., M.R.V. Ross., N.E. Clinton., D.J. Campagna., Y. Franklin., E.S. Bernhardt., and J.F. Amos.,** 2018
Mapping the yearly extent of surface coal mining in Central Appalachia using Landsat and Google Earth Engine, PLOS ONE, Vol. 13, No. 7. DOI: 10.1371/journal.pone.0197758.

[33] Firozjaei, M.K., A. Sedighi., H.K. Firozjaei., M. Kiavarz., M. Homaee., J.J. Arsanjani., M. Makki., B. Naimi., S.K. Alavipanah., 2021
A historical and future impact assessment of mining activities on surface biophysical characteristics change: A remote sensing-based approach, Ecological Indicators, Vol. 122, 107264. DOI: https://doi.org/10.1016/j.ecolind.2020.107264.

[34] **Xulu, S., P.T. Phungula., N. Mbatha., and I. Moyo.,** 2021
Multi-Year Mapping of Disturbance and Reclamation Patterns over Tronox's Hillendale Mine, South Africa with DBEST and Google Earth Engine, Land, Vol. 10, No. 7, 760 DOI: https://doi.org/10.3390/land10070760

[35] **Tucker, C.J.,** 1979
Red and photographic infrared linear combinations for monitoring vegetation, Remote Sensing of Environment, 1979. Vol. 8, No. 2,127-150. DOI: https://doi.org/10.1016/0034-4257(79)90013-0.

[36] **Kennedy, R.E., Z. Yang., N. Gorelick., J. Braaten., L. Cavalcante., W.B. Cohen., and S. Healey.,** 2018
Implementation of the LandTrendr Algorithm on Google Earth Engine, Remote Sensing, Vol. 10, No. 5, 691. DOI: https://doi.org/10.3390/rs10050691

[37] **de Jong, S.M., Y. Shen., J. de Vries., G. Bijnaar., B. van Maanen., P. Augustinus., and P. Verweij.,** 2021
Mapping mangrove dynamics and colonization patterns at the Suriname coast using historic satellite data and the LandTrendr algorithm, International Journal of Applied Earth Observation and Geoinformation, Vol. 97, 102293. DOI: https://doi.org/10.1016/j.jag.2020.102293.

[38] **Kennedy, R.E., Z. Yang., and W.B. Cohen.,** 2010
Detecting trends in forest disturbance and recovery using yearly Landsat time series: 1. LandTrendr — Temporal segmentation algorithms, Remote Sensing of Environment, Vol. 114, No. 12, 2897-2910 DOI: https://doi.org/10.1016/j.rse.2010.07.008.

[39] **Zhu, L., X. Liu., L. Wu., Y. Tang., and Y. Meng.,** 2019
Long-Term Monitoring of Cropland Change near Dongting Lake, China, Using the LandTrendr Algorithm with Landsat Imagery, Remote Sensing, Vol. 11, No. 10, 1234. DOI: https://doi.org/10.3390/rs11101234

[40] **Yang, Y., P.D. Erskine., A.M. Lechner., D. Mulligan., S. Zhang., and Z. Wang.,** 2018
Detecting the dynamics of vegetation disturbance and recovery in surface mining area via Landsat imagery and LandTrendr algorithm, Journal of Cleaner Production, Vol. 178, 353-362. DOI: https://doi.org/10.1016/j.jclepro.2018.01.050.

[41] **Breiman, L.,** 2001
Random Forests, Machine Learning, (2001), 45(1), 5-32. DOI: 10.1023/A:1010933404324.

[42] **Congalton, R., and K. Green.,** 2019
Assessing the Accuracy of Remotely Sensed Data: Principles and Practices, Third Edition, DOI: 10.1201/9780429052729.

[43] **Rodriguez-Galiano, V.F., B. Ghimire., J. Rogan., M. Chica-Olmo., and J.P. Rigol-Sanchez.,** 2012
An assessment of the effectiveness of a random forest classifier for land-cover classification, ISPRS Journal of Photogrammetry and Remote Sensing, Vol. 67, 93-104. DOI: https://doi.org/10.1016/j.isprsjprs.2011.11.002.

[44] **Lange, M., H. Feilhauer., I. Kühn., and D. Doktor.,** 2022
Mapping land-use intensity of grasslands in Germany with machine learning and Sentinel-2 time series, Remote Sensing of Environment, Vol. 277, 112888. DOI: https://doi.org/10.1016/j.rse.2022.112888.

[45] **Yu, X., K. Zhang., and Y. Zhang.,** 2022
Land use classification of open-pit mine based on multi-scale segmentation and random forest model, PLOS ONE, Vol. 17, No. 2, 263870. DOI: 10.1371/journal.pone.0263870.